mining

MDPI

Article

Rock Mass Risk Assessment Coupling Microseismic Monitoring with Mining–Filling Data: A Deep Mine Case Study from the Sishanling Iron Mine

Xiaodong Wang [1] and Congcong Zhao [2,3,*]

[1] Benxi Longxin Mining Co., Ltd., Group 1, Sishanling Subdistrict, Nanfen District, Benxi 117013, China
[2] School of Resources and Safety Engineering, University of Science and Technology Beijing, No. 30 Xueyuan Road, Haidian District, Beijing 100083, China
[3] China Academy of Safety Science and Technology, No. 32 Beiyuan Road, Chaoyang District, Beijing 100012, China
* Correspondence: congcongzhao@ustb.edu.cn

Abstract

The intensification of ground pressure and instability of surrounding rock in deep mining are the core safety challenges of metal mines. This article takes the first mining area of the Sishanling Iron Mine from 960 m to 1020 m as the object, and based on the data obtained from the multi-channel microseismic monitoring system for the whole year of 2025, combined with monthly mining and filling parameters, conducts a rock mass risk assessment that couples microseismic activity with the mining and filling process. The results show that microseismic activity and blasting operations exhibit a significant "resonance of the same frequency" response. The event-intensive areas are distributed along the fault zone and the edge of the goaf, and migrate in a directional manner from shallow to deep with the advancement of mining. By comparing the photos of the tunnel damage on site on a monthly basis, it was found that the incident gathering area was highly consistent with the locations of roof collapse and debris support, which verified the accuracy of microseismic positioning. Based on this, a risk discrimination index based on event frequency, energy release rate, and spatial concentration was established to dynamically evaluate the −960 m and −1020 m sections on a monthly basis. The local risk intensity in the −1020 m section was higher, and the risk increased compensatorily when the filling was delayed 2–4 weeks after mining, revealing the key control role of the mining filling coordination rhythm on the stability of the surrounding rock. The coupled evaluation system of mining filling microseismic risk constructed in this study can provide technical reference for active early warning and differentiated prevention and control of ground pressure in deep mines.

Keywords: deep hard rock mines; microseismic activity; mining filling coupling; rock mass stability; risk assessment

Check for updates

Academic Editor: Chaoshui Xu

Received: 14 August 2026
Revised: 13 September 2026
Accepted: 15 September 2026
Published: 17 September 2026

Copyright: © 2026 by the authors. Licensee MDPI, Basel, Switzerland. This article is an open access article distributed under the terms and conditions of the Creative Commons Attribution (CC BY) license.

1. Introduction

The intensification of ground pressure and instability of surrounding rock in deep mining is one of the core challenges faced by metal mines [1]. As the mining depth increases, the original rock stress rises sharply, and the surrounding rock of tunnels in high stress concentration areas often experiences sudden fractures or even rock bursts without obvious warning, seriously threatening the safety of operators and equipment [2,3]. As a typical

deep well mine in China, the first mining area of Sishanling Iron Mine is located at the level of −960 m to −1020 m. This area plays an important role in capacity continuity, but at the same time, it is also located in the core area of high ground stress, and the stability of the roadway is particularly prominent [4].

Traditional rock stability monitoring mainly relies on point contact sensors such as stress gauges or displacement gauges. Although these methods can reflect the stress changes at local measurement points, they are unable to capture the complete spatiotemporal evolution process of rock fracture, and they cannot meet the real-time three-dimensional tracking needs of rock damage under large-scale mining disturbances [5]. The initiation and propagation of microcracks in underground rock masses are common problems in mining and oil and gas development. In recent years, significant progress has been made in numerical simulation research on the crack propagation behavior of unconventional reservoirs. For example, Li et al. [6] analyzed the crack propagation behavior and influencing factors of CO_2 fracturing fluid in low-permeability reservoirs, while Feng et al. [7] systematically studied the crack propagation mode and sensitivity factors of oil shale reservoirs in the Xunyi area by combining the influence of natural cracks. These works provide important references for understanding the fracture mechanism of rocks under complex stress conditions. In contrast, microseismic monitoring technology can achieve three-dimensional positioning and quantitative energy analysis of the entire process of rock microcrack initiation, propagation, and penetration by capturing the elastic waves released during rock fracture. It has significant advantages such as wide coverage, sensitive response, and advanced warning [8]. Therefore, relying on the existing microseismic monitoring system in the first mining area of Sishanling Iron Mine, capturing real-time response information of surrounding rock fractures, and providing basic data support for subsequent disaster warning and risk control has important engineering practical significance [9].

However, current research on microseismic monitoring in the deep middle section of the Sishanling Iron Mine mainly relies on short-term data analysis or local event description, lacking a long-term series (such as annual scale) systematic evaluation covering the entire mining cycle, and a dynamic risk level evaluation system for tunnels based on coupling annual microseismic activity and production data has not yet been established [10,11]. This research gap directly restricts the transformation of deep disaster prevention and control in the mine from "passive rescue" to "active warning" [12,13]. Therefore, based on the established microseismic monitoring system in the mine, this article collected and processed microseismic signals for the whole year of 2025. Based on the P-wave/S-wave arrival-time positioning calculation, the spatial three-dimensional distribution of microseismic events was obtained, and further statistical analysis was conducted on the cumulative energy of rupture events and the evolution of microseismic signal numbers over time [14]. In this context, stress-field detection and quantitative characterization methods based on microseismic data have also been explored for dynamic hazard prediction [15,16]. Meanwhile, by combining monthly production plans with mining and filling data, the temporal response relationship between mining activity intensity and microseismic activity was analyzed to reveal the dominant role of mining disturbance in the evolution of surrounding rock fracture [17]. On the spatial dimension, microseismic events are grouped and displayed by month, clearly outlining the migration pattern of rupture zones as mining progresses [18]. At the same time, by comparing the photos of tunnel damage recorded on site on a monthly basis, the spatial correspondence between microseismic gathering areas and actual damage locations was clarified [19,20].

On the basis of the above analysis, this article introduces the classification of roadway risk levels [21,22], and combines corresponding damage types and prevention and control measures to conduct monthly risk assessments of the roadway in the −960 m and −1020 m

sections, respectively. Finally, the reliability of the evaluation results was verified by closely comparing the spatial distribution of microseismic events during typical periods with the on-site damage situation. This study aims to fill the research gap in the annual-scale microseismic risk dynamic evaluation of Sishanling Iron Mine. The research results can provide direct technical reference for dynamic disaster prevention and control in the deep mining area of the mine, and accumulate systematic practical experience for the construction of a microseismic monitoring and risk assessment system in similar deep well mines.

2. Project Overview and Monitoring System

2.1. Overview of Engineering Geology

The Sishanling Iron Mine is located in the northeastern margin of the North China Plate in the Benxi area of Liaoning Province. Structurally, it belongs to the central southern part of the Liaoyang Benxi Depression, which includes the mid-stage quasi-platform Jiaoliao Tailong Taizihe Hunjiang Platform Depression. The ore body is hosted in the Anshan Group strata of the Precambrian period and belongs to the Anshan-style sedimentary metamorphic iron ore (banded ferrite). The main rock layers in the mining area include mixed rocks, iron-bearing quartzite series, and later intrusive igneous rocks such as diabase and diorite. The burial depth of the ore body ranges from 404 m to 1934 m, and it belongs to a typical deep well mine. This article takes the first mining area of the mine at the level of −960 m to −1020 m (Figure 1) as the research object. The mining area is located in the key occurrence section of the deep ore body. The rock mechanics test shows that the average compressive strength of diorite is 100.8 MPa, the average compressive strength of hematite quartzite is 131.0 MPa, and the average compressive strength of magnetite quartzite is 126.94 MPa. The overall hardness and integrity of the ore and surrounding rock are high, and there are no large-scale structural fracture zones in the deep rock mass. Only small-scale cracks are locally developed, providing a relatively complete rock foundation for deep mining.

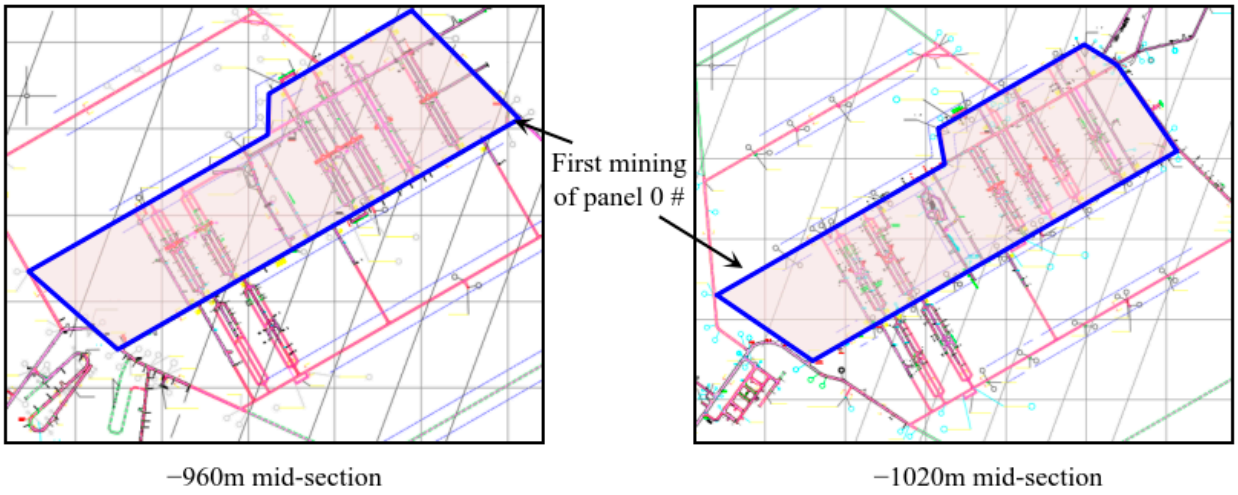


Figure 1. The first mining area at the −960 m~−1020 m level of Sishanling Iron Mine.

Based on the in-situ stress environment of the first mining area mentioned above, the measured results of the hydraulic fracturing method show that the area is in a deep high-stress state, with the maximum horizontal principal stress being the first principal stress, which is stable in the near NEE direction and has an average azimuth angle of about 67.83°; Each principal stress component (maximum horizontal principal stress, minimum horizontal principal stress, and vertical principal stress) shows an approximately linear

growth trend with increasing burial depth. When the burial depth exceeds one kilometer, the ratio of the maximum to minimum horizontal principal stresses in the surrounding rock is about 1.58, and the ratio in the ore body is about 1.46, indicating that the rock mass where the first mining area is located is in a strongly anisotropic high-stress state. This significant difference in principal stresses constitutes a significant cause of potential instability in deep mining. In addition, the measured data at a depth of over 1000 m show that the horizontal principal stress of the surrounding rock is about 1.06 times that of the ore body, which means that the stress of the surrounding rock is slightly higher than that of the ore body. This stress difference characteristic has direct engineering guidance significance for the layout of the mining area, roadway support, and stability control of the surrounding rock in the −960 m to −1020 m first mining area.

2.2. Layout Plan for Microseismic Monitoring System

This project has developed a high-precision microseismic monitoring system to address the stability issues of the rock mass during the mining process at the −1033~−1060 m level. The system uses a three-component velocity sensor with a bandwidth response range of 0.5~5000 Hz, and its sensitivity is no less than 30 V/(m/s), which can effectively capture high-frequency seismic wave signals generated by rock microfractures. Combined with the humid and high rock pressure working environment underground, the sensor housing has a protection level of IP67 and is equipped with low-noise shielded cables to ensure the fidelity of signals during long-distance transmission. The data acquisition station adopts a 24-bit A/D converter with a sampling frequency set to 6000 Hz to meet the frequency band requirements for precise positioning of microseismic events and analysis of source mechanisms.

In terms of deployment principles, the design of the monitoring network strictly follows the spatial enclosure optimization strategy. Firstly, the sensor array must effectively wrap around the monitored mining site and key surrounding rock areas in three-dimensional space, avoiding all measurement points being located on the same side of the seismic source to reduce the ill-conditioning of the positioning system matrix. Secondly, taking into account the layout of underground tunnels, rock integrity, and construction operability, sensors are buried in the moderately weathered bedrock on both sides of the tunnel, with a burial depth controlled at around 5.0 m, to ensure good coupling between the sensors and the surrounding rock. At the same time, the equivalent propagation velocity of the P-wave in this section is determined through wave velocity testing and calibration experiments, providing an accurate initial velocity model for subsequent positioning algorithms and controlling the overall positioning error of the system within ±10 m. It should be noted that the localization procedure in this study is based solely on P-wave and S-wave arrival-time differences; no full-waveform inversion or moment tensor analysis was performed or moment tensor analysis was performed. The term "positioning" here refers strictly to hypocenter determination via arrival-time picking, and the spatial distributions presented in following text represent event locations derived from this method.

Figure 2 shows the overall layout path of the underground cables for the horizontal microseismic monitoring system. As shown in the figure, the main signal cable is installed along the side wall of the transportation roadway, using an armored shielding structure to prevent mechanical damage and electromagnetic interference. At each branch point, the sensor signals are collected to the data acquisition substation through waterproof junction boxes. The wiring structure combining the ring network with tree branches not only ensures independent transmission channels for signals at each measurement point, but also facilitates later partition expansion and maintenance. Figure 3 presents the hardware

architecture of the existing microseismic monitoring system at the −1033~−1060 m level, clearly identifying the hierarchical relationship between the data acquisition station, timing synchronization module (GPS/Beidou), Ethernet switch, and central analysis server, revealing the entire physical link of signal acquisition from sensors, analog–to–digital conversion, and data transmission to the ground analysis center.

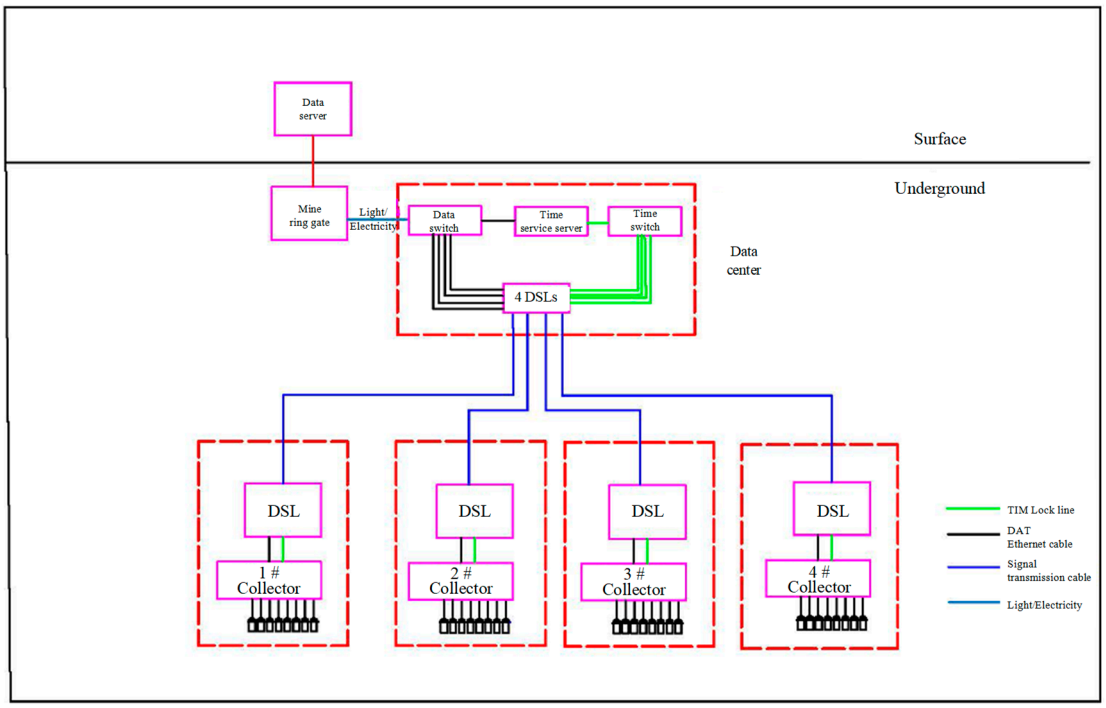


Figure 2. Layout of underground cables for microseismic monitoring.

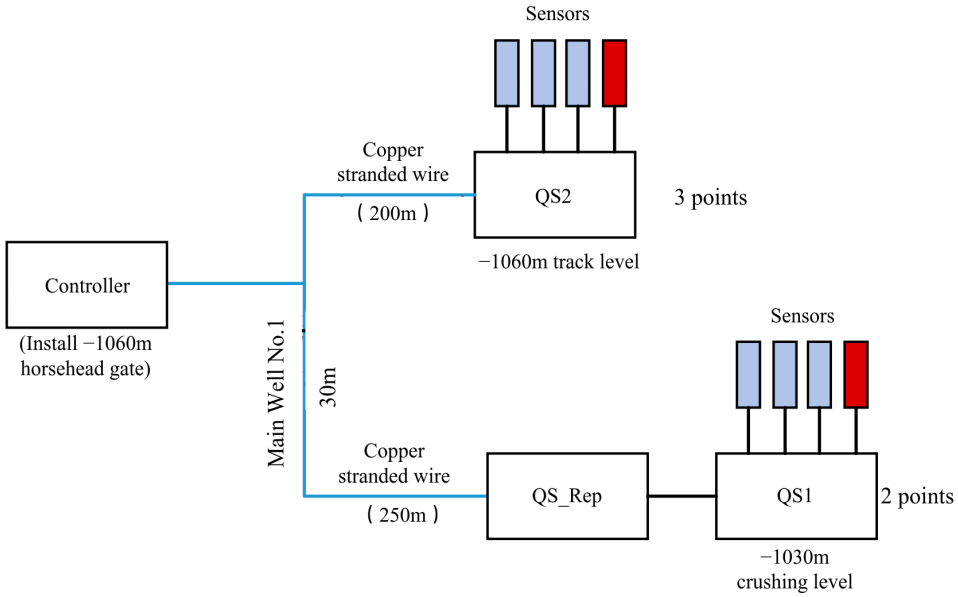


Figure 3. m horizontal existing microseismic monitoring system. (The red color indicates reserved sensor channels).

In terms of coverage, the system is equipped with 5 velocity sensors in the horizontal range of −1033 to −1060 m, with coverage spans of 480 m and 320 m in the strike and dip directions, respectively. It covers all mining areas in the middle section in the vertical direction. Figure 4 shows the specific burial location and drilling profile layout details

of existing sensors on this horizontal plane. From the figure, it can be seen that sensors are not arranged at equal intervals, but are non uniformly densified based on the boundaries of the goaf and the spatial distribution of faults. The distance between measuring points in the fault influence zone and on both sides is reduced to about 40–50 m to achieve high-resolution monitoring of key risk areas. By three-dimensional calculation of sensor coordinates, the expected accuracy of seismic source positioning in the area can be ensured to meet the engineering warning threshold requirements, providing a reliable data foundation for real-time assessment and active prevention and control of mining dynamic disasters.

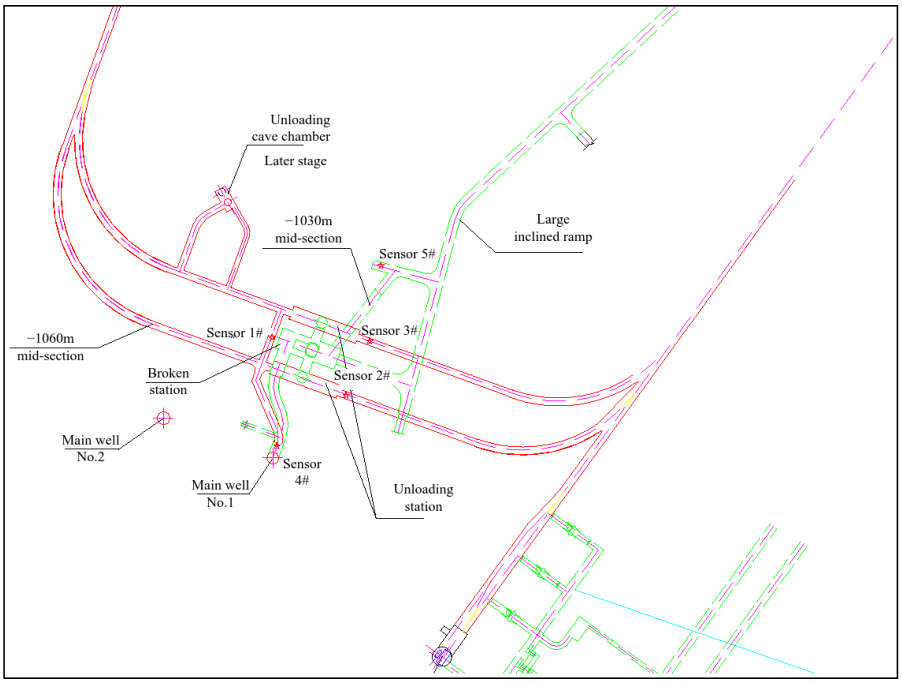


Figure 4. Horizontal existing sensor burial layout.

3. Monitoring Data Foundation and Production Parameters

This section aims to establish an engineering connection between microseismic monitoring data and production activities, providing data support for subsequent energy release anomalies and disaster risk assessments. Firstly, present the spatial distribution pattern of annual microseismic events from a macro perspective, then reveal the controlling effect of production intensity on microseismic activity through time series analysis, and finally supplement monthly data collection and filling to improve the engineering background.

3.1. Spatiotemporal Distribution Characteristics of Microseismic Events

The spatial distribution of microseismic events throughout the year shows significant non-uniformity, with event-intensive areas mainly distributed along known fault structural zones and forming surrounding gathering zones at the edges of goaf areas. This distribution pattern indicates that the existing structural planes have undergone significant stress redistribution under mining stress disturbance, and the vicinity of the fault zone has become a high-risk area for microseismic events. The boundary of the goaf, on the other hand, has experienced stress concentration in the surrounding rock due to unloading effects, which also constitutes a favorable location for event density.

From the perspective of three-dimensional hypocenter locations determined by P/S arrival-time positioning (Figure 5), there is good consistency between the nucleation location of the event and the direction of mining face advancement, indicating that the disturbance of the surrounding rock stress field correlated with current mining activities

has extended to the vicinity of the fault. The appearance of local microseismic clusters suggests the activation trend of weak structural planes under mining influence. Overall, the maximum discrete range of event spatial distribution covers the main mining middle section, while the vertical distribution span reflects the superposition effect of multi–level mining activities. From the perspective of magnitude, larger magnitudes tend to cluster more prominently in deep areas, with very few in the upper part and closely distributed in production areas in the lower part.

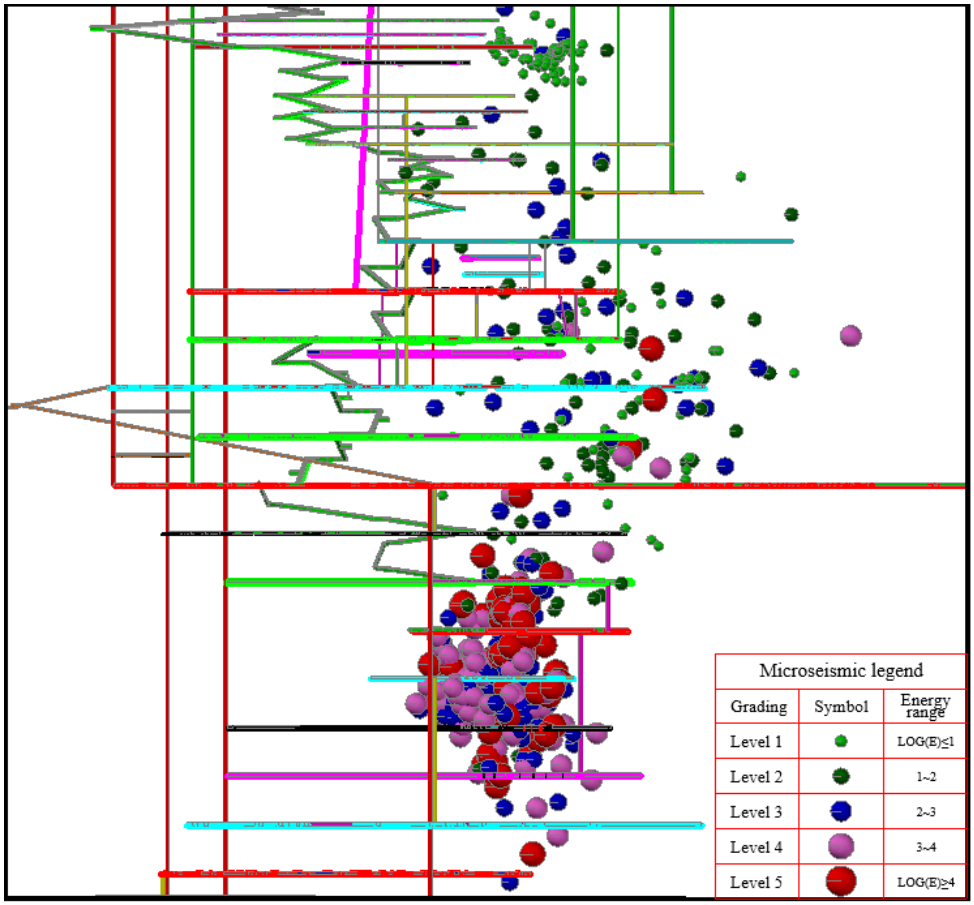


Figure 5. Three-dimensional display of spatial location of microseismic events.

To characterize the statistical nature of the microseismic event occurrence, a distribution analysis was performed on the daily event count series. The Kolmogorov–Smirnov goodness-of-fit test was applied to examine whether the event counts follow a Poisson distribution, which is commonly assumed for random, independent point processes. The test results rejected the Poisson hypothesis at the 95% confidence level ($p < 0.01$) for most monthly datasets, indicating that the event occurrence exhibits significant over-dispersion and clustering behavior. This non-Poissonian nature, characterized by a variance-to-mean ratio substantially greater than unity (ranging from 2.1 to 5.8 across different months), confirms that microseismic events are not randomly distributed but are strongly influenced by mining activities and structural discontinuities. This clustering behavior justifies the use of empirical thresholds rather than parametric statistical limits based on normal or Poisson assumptions. The natural breaks optimization method adopted in Section 4.2 is particularly suitable for such non-Gaussian, multi-modal distributions, as it does not rely on any predefined probability distribution.

3.2. Correlation Analysis Between Production Activities and Microseismic Activities

To ensure that the observed microseismic activity truly reflects the response of the rock mass, rather than the vibration correlated with direct explosions, a strict signal classification protocol has been implemented. All raw waveforms recorded by the monitoring system are first automatically detected using short-term/long-term averaging (STA/LTA) triggering algorithms for event identification and arrival-time picking. The subsequent hypocenter determination is based exclusively on P-wave and S-wave arrival-time differences; no moment tensor location by arrival times or focal mechanism analysis is conducted in this study, and the results are then manually verified by experienced analysts. The classification criteria are as follows:

Identify signals correlated with explosions based on the following diagnostic features: (1) high amplitude and short duration (usually <0.5 s), (2) main frequency <50 Hz, (3) multiple sensors with consistent polarity triggered simultaneously, and (4) known blasting plans provided by the mining production department. These events are excluded from the microseismic event catalog used for subsequent risk analysis.

The characteristics of a true microseismic event (rock fracture) are: (1) low amplitude, long rise time, (2) wide frequency content (50–5000 Hz), (3) more localized sensor triggering mode, (4) obvious waveform features, with P-waves and S-waves arriving without high-energy low-frequency "air explosion" characteristics.

The parameter 'blasting volume' is defined as the total tonnage of ore extracted through blasting operations during a given period, expressed as 10,000 t (10^4 t) per month. This includes ore and waste rock crushed and removed from the mining site, consistent with the "Mining Production" column in Table 1.

Table 1. Monthly production plan for 2025.

Category	The Tonnage of Mining					Filling Volume	Other	
Project	Gross Weight /10^4 t	Weight with Rock /10^4 t	Weight with Ore /10^4 t	Mining Output /10^4 t	Pure Ore Weight /10^4 t	Filling /10^3 m^3	Total Tailings Weight /10^4 t	Tailings Weight for Filling /10^4 t
Jan.	55.79	1.07	7.89	46.83	54.72	7.02	36.37	9.62
Feb.	53.87	0.98	7.65	45.23	52.88	7.13	35.02	9.77
Mar.	53.87	0.8	7.13	45.93	53.07	8.8	34.88	12.06
Apr.	50.02	0.9	7.41	41.72	49.12	10.38	31.96	14.22
May.	59.64	0.82	7.2	51.61	58.81	10.1	38.27	13.84
Jun.	57.71	0.87	7.32	49.53	56.85	12.33	36.89	16.89
Jul.	48.1	0.93	7.49	39.68	47.17	12.53	30.4	17.17
Aug.	50.02	0.82	7.19	42	49.2	12.37	31.3	16.95
Sep.	57.71	0.8	7.14	49.77	56.91	15.05	35.96	20.62
Oct.	59.64	0.79	7.1	51.75	58.85	15.04	37.19	20.6
Nov.	51.94	0.98	7.65	43.31	50.96	17.04	32.44	23.34
Dec.	51.94	0.83	7.19	43.92	51.11	17.18	32.94	23.54
Total	650.25	10.6	88.37	551.29	639.66	144.97	413.61	198.61

The empirical observation of the 2–4 h post-explosion monitoring window for the increase in microseismic activity comes from the time decay analysis of the event occurrence rate after 158 individual explosion records in 2025. Figure 6 (inset) shows the variation of normalized microseismic event rate over time after blasting, indicating that approximately 72% of rock fracture events occur within the first 4 h after blasting, with peak activity

concentrated in the interval of 0–2 h. This time window reflects the typical duration of stress redistribution and strain energy release around the excavation front after the explosion, rather than arbitrary selection. Therefore, it is recommended to use 2–4 h as the actual monitoring interval for post-explosion hazard assessment, during which the probability of delayed rock fracture significantly increases.

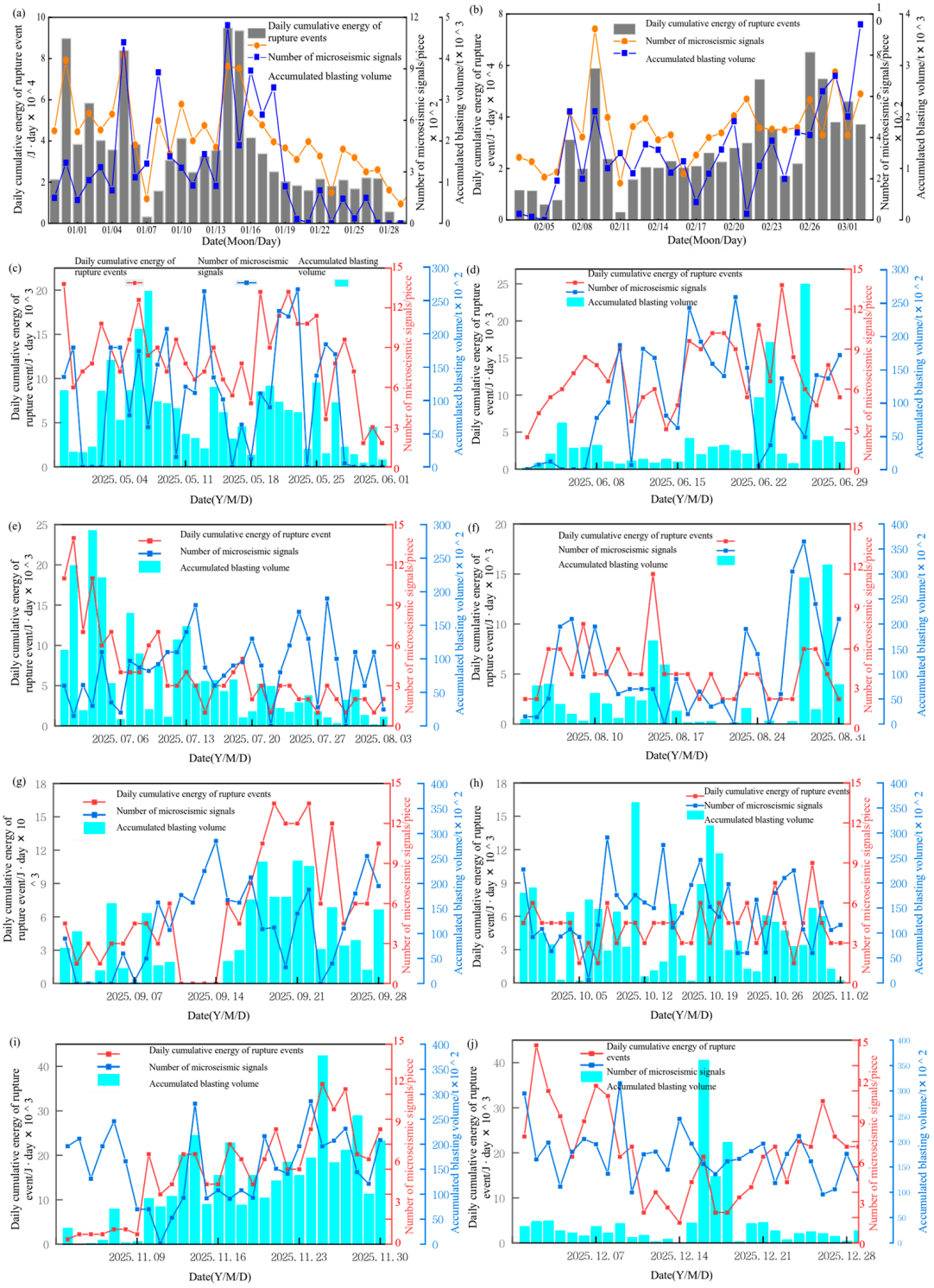


Figure 6. Time series diagram of the relationship between cumulative energy of rupture events, microseismic signal numbers, and blasting volume. (**a**,**b**) show the data for January and February 2025; (**c**–**j**) show the data from May to December.

There is a clear characteristic of "resonance at the same frequency" between the temporal evolution of microseismic activity and the production rhythm. Blasting operations, as the main source of engineering disturbance, directly trigger the vast majority of detectable microseismic events. Figure 6 clearly shows this correlation: during the shutdown or low production period from January to February, the cumulative energy curve tends to flatten out, and the number of microseismic signals remains at a low level; After entering the high production period from May to December, the amount of blasting and microseismic signals increased synchronously, and the energy release curve showed a step-like jump. After each round of concentrated blasting operations, there was a significant response in microseismic frequency and energy.

From the perspective of fluctuation patterns, energy release exhibits phased characteristics with changes in production intensity. The stable curve during low production periods contrasts sharply with the sharp rise during high production periods, fully demonstrating that the intensity of mining activities directly controls the overall level of microseismic activity. It is worth noting that the relative increase in energy release exceeds the increase in blasting volume during certain periods, which suggests the possibility of secondary rupture induced by stress adjustment, in addition to direct blasting triggering. Blasting not only produces immediate elastic wave release, but also may break local stress balance, triggering subsequent secondary microseismic events. From the time series relationship chart between energy/signal number and blasting volume, it can be seen that there is a clear correspondence between the low production period from January to February and the high production period from May to December: when the total blasting volume increases, the total number of microseismic signals and the cumulative released energy both show a synchronous upward trend. This indicates that blasting operations and the surrounding rock disturbance they cause are the dominant factors triggering microseismic activity, and the level of energy release fluctuates dynamically with changes in production intensity.

3.3. Monthly Evolution Trend

From a monthly perspective, the spatial distribution of microseismic events exhibits an evolutionary pattern of gradual migration from shallow to deep, and from the center of the mining site to the two side boundaries (Figure 7a–k). Events in January and February were sporadically distributed in the residual stress adjustment zone of the mining area, with low event density and scattered spatial distribution, reflecting only a slow process of stress redistribution during the shutdown period. With the resumption of production in April, the event began to nucleate near the mining face that year, and the dense area gradually moved closer to the production active area.

During the period of May to December, the event-intensive area showed a clear directional migration trajectory along the direction of the ore body, which was closely related to the direction and speed of the mining face. The location of the advantageous gathering area each month basically corresponded to the mining front line of that month. By the end of the year (Figure 7), the cumulative spatial envelope of events throughout the year basically outlined the scope of mining impact, and the spatial concentration of events reached its peak in December, indicating that the stress concentration of surrounding rock in the goaf continued to increase with the expansion of mining scale. This spatial migration trend provides important spatiotemporal direction for subsequent warning.

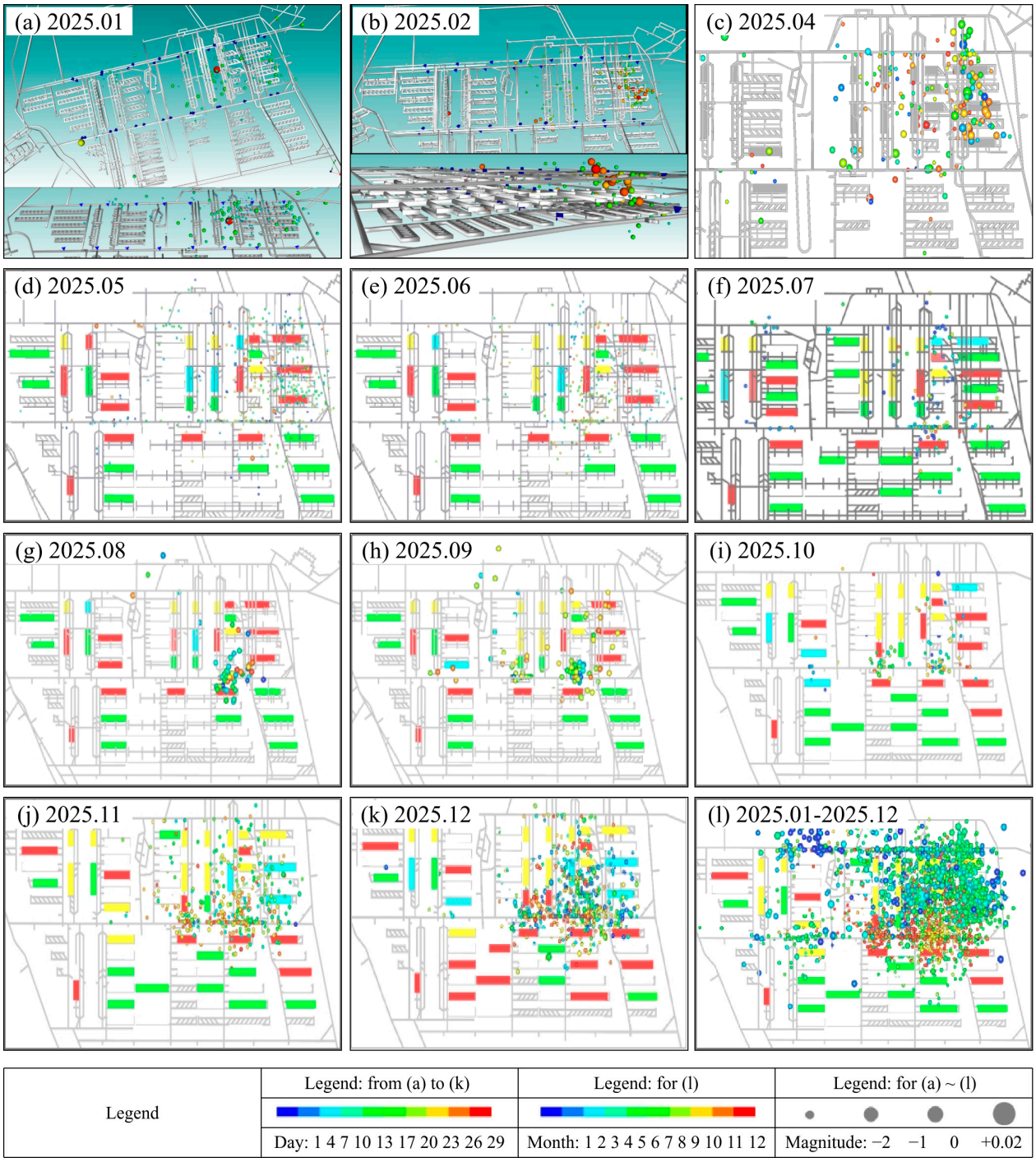


Figure 7. Spatial distribution map of microseismic events. (**a**–**k**): Monthly spatial distribution maps for January, February, April, and December 2025; (**l**) annual summary of 2025.

3.4. Analysis of Production Intensity Data

To quantitatively characterize the driving effect of production activities on microseismic response, we analyzed the annual mining and filling data (Tables 2 and 3, with monthly production plans shown in Table 1). The monthly distribution of mining volume reflects the rhythm changes of mining progress, with a sharp contrast in intensity between the shutdown or low production period from January to February and the high production period from May to December. This trend of change is completely consistent with the temporal characteristics of microseismic activity mentioned above on the timeline.

Table 2. Mining data for 2025 (unit/10,000 t).

No.	Mining Site Number	Jan.	Feb.	Mar.	Quarter 1	Apr.	May.	Jun.	Quarter 2	Jul.	Aug.	Sep.	Quarter 3	Oct.	Nov.	Dec.	Quarter 4	Total
First: Stage mining site																		
1	0#-8-1/2				0.0				0.0				0.0				0.0	0.0
2	0#-8-3			1.3	1.3	6.0	5.5		11.5				0.0				0.0	12.8
3	0#-8-5				0.0				0.0				0.0				0.0	0.0
4	0#-8-4				0.0				0.0	1.3	3.0	6.0	10.3	3.8			3.8	14.1
5	0#-8-3 (P)				0.0				0.0				0.0	1.3	6.0	6.0	13.3	13.3
6	0#-12-1/2				0.0				0.0				0.0				0.0	0.0
7	0#-12-3				0.0	1.3	3.0	6.0	10.3	2.5			2.5				0.0	12.8
8	0#-12-5				0.0				0.0				0.0				0.0	0.0
9	0#-12-4				0.0				0.0		1.3	3.0	4.3	6.0	3.8		9.8	14.1
10	0#-12-3 (P)				0.0				0.0				0.0		1.3	6.0	7.3	7.3
11	0#-16-1/2	3.0	3.0	6.0	12.0	6.0	4.5	1.6	12.1				0.0				0.0	24.1
12	0#-16-3				0.0				0.0				0.0			1.3	1.3	1.3
13	0#-16-5	6.0	6.0	0.8	12.8				0.0				0.0				0.0	12.8
14	0#-16-4				0.0				0.0				0.0				0.0	0.0
15	0#-16-3 (P)				0.0				0.0				0.0				0.0	0.0
16	0#-7-1/2				0.0				0.0	4.7	4.3	6.0	15.0	6.0	1.1		7.1	22.1
17	0#-7-3				0.0				0.0				0.0				0.0	0.0
18	0#-7-5				0.0				0.0				0.0				0.0	0.0
19	0#-7-4																	
20	0#-11-1/2	2.0			2.0				0.0				0.0				0.0	2.0
21	0#-11-5				0.0				0.0				0.0				0.0	0.0
22	0#-11-4				0.0				0.0		1.3	3.0	4.3	4.5	5.3		9.8	14.1
23	0#-11-3 (P)				0.0				0.0				0.0		1.3	6.0	7.3	7.3
Subtotal		11.0	9.0	8.1	28.1	13.3	13.0	7.6	33.9	8.5	9.9	18.0	36.4	21.6	18.8	19.3	59.7	158.1
Second: Segmented mining site																		
1	0-26-9	6.0	6.0	5.4	17.4				0.0				0.0				0.0	17.4
2	0-26-5	4.5	4.5	4.5	13.5	6.0	4.3		10.3				0.0				0.0	23.8

Table 2. *Cont.*

No.	Mining Site Number	Jan.	Feb.	Mar.	Quarter 1	Apr.	May.	Jun.	Quarter 2	Jul.	Aug.	Sep.	Quarter 3	Oct.	Nov.	Dec.	Quarter 4	Total
3	0-26-1				0.0		2.0	2.0	4.0	2.0	6.0	6.0	14.0	3.1	3.0	3.0	9.1	27.1
4	0-26-7				0.0				0.0				0.0		1.3		1.3	1.3
5	0-20-5				0.0			3.5	3.5	3.2	3.2	4.5	10.9				0.0	14.4
6	0-20-1				0.0			2.0	2.0	3.0	5.8		8.8				0.0	10.8
7	0-2-10				0.0				0.0				0.0	1.3			1.3	1.3
8	0-2-6				0.0				0.0			1.3	1.3				0.0	1.3
9	0-2-2				0.0				0.0		1.3	3.0	4.3	3.0	3.2	3.0	9.2	13.5
10	2-22-9			1.3	1.3				0.0				0.0				0.0	1.3
11	2-22-5			1.3	1.3				0.0				0.0	2.0	3.0	3.5	8.5	9.8
12	2-22-1	4.1	4.1	4.1	12.3	3.0	3.0	4.5	10.5	4.5	1.7		6.2				0.0	29.0
13	2-20-9				0.0			1.3	1.3				0.0				0.0	1.3
14	2-20-5				0.0	1.3			1.3				0.0	3.0	4.5	4.5	12.0	13.3
15	2-20-1	2.3	3.5	4.0	9.8	4.0	4.0	4.0	12.0	3.0			3.0				0.0	24.8
16	2-12-11				0.0				0.0		1.3		1.3				0.0	1.3
17	2-12-7				0.0				0.0	1.3			1.3				0.0	1.3
18	2-12-3				0.0		1.3		1.3				0.0				0.0	1.3
19	0-5-10	6.0	6.0	0.6	12.6				0.0				0.0				0.0	12.6
20	0-5-6	3.0	3.0	3.0	9.0	6.0	6.0	6.0	18.0	2.3			2.3				0.0	29.3
21	0-5-8				0.0				0.0				0.0		1.3	2.5	3.8	3.8
22	0-5-4				0.0				0.0				0.0		1.3	2.5	3.8	3.8
23	0-15-7			1.3	1.3	1.1	1.1	1.1	3.3	1.1	1.1	2.6	4.8	3.1	3.1	3.7	9.9	19.3
24	0-15-3				0.0			1.3	1.3				0.0	3.0	3.0	3.6	9.6	10.9
25	1-15-1				0.0				0.0				0.0		1.3		1.3	1.3
26	1-15-4				0.0				0.0				0.0				0.0	0.0
27	1-17-3				0.0				0.0				0.0				0.0	0.0
28	2-5-1	3.0	3.0	6.0	12.0	6.0	5.1		11.1				0.0				0.0	23.1
29	2-5-5	1.7	3.0	3.0	7.7	3.0	3.0	6.0	12.0	6.0	3.3		9.3				0.0	29.0
30	2-5-9			1.3	1.3				0.0				0.0				0.0	1.3

Table 2. *Cont.*

No.	Mining Site Number	Jan.	Feb.	Mar.	Quarter 1	Apr.	May.	Jun.	Quarter 2	Jul.	Aug.	Sep.	Quarter 3	Oct.	Nov.	Dec.	Quarter 4	Total
31	2-11-1/2	3.0	2.7	2.7	8.4	2.2	2.2	2.2	6.6	4.7	4.2	3.7	12.6	2.5			2.5	30.1
32	2-4-1				0.0		1.3	4.5	5.8	4.5	6.0	6.0	16.5	0.9			0.9	23.2
33	2-2-11				0.0				0.0				0.0				0.0	0.0
34	2-2-7				0.0				0.0		1.3		1.3				0.0	1.3
35	2-2-3				0.0				0.0	1.3	1.0	1.0	3.3	2.6	2.0	2.0	6.6	9.9
Subtotal		33.6	35.8	38.5	107.9	32.6	33.3	38.4	104.3	36.9	36.2	28.1	101.2	24.5	27.0	28.3	79.8	393.2
Total		46.8	45.2	45.9	138.0	41.7	51.6	49.5	142.9	39.7	42.0	49.8	131.5	51.8	43.3	43.9	139.0	551.3

Table 3. Filling data for 2025 (unit/10,000 m^3).

Mining Location	Mining Site Number	Volume of Goaf in Mining Area	Jan.	Feb.	Mar.	Apr.	May.	Jun.	Jul.	Aug.	Sep.	Oct.	Nov.	Dec.	Total
First: Stage mining site	0#-8-1/2	7.80	2.2	2.2	1.4										5.8
	0#-8-3	4.30						0.7	1.3	1.3	1.1				4.3
	0#-8-5	4.40													0.0
	0#-8-4	4.37											0.5	1.7	2.2
	0#-12-1/2	7.15	1.5	2.1	2.1	1.5									7.2
	0#-12-3	4.29								0.8	1.3	1.6	0.5		4.2
	0#-12-5	4.39	1.1												1.1
	0#-12-4	4.42												1.1	1.1
	0#-16-1/2	7.72						1.6	2.2	2.2	1.8				7.7
	0#-16-5	4.45			0.9	1.5	1.9	0.3							4.5
	0#-7-1/2	7.33												1.8	1.8
	0#-7-5	4.25	1.0	1.2	1.2	1.0									4.3
	0#-11-1/2	7.54		0.5	2.3	3.0	1.5								7.3
	0#-11-5	4.38	1.3	1.2	1.0										3.5
	0#-11-4	4.46												0.9	0.9
	Subtotal		7.0	7.1	8.8	6.9	3.4	2.5	3.5	4.3	4.1	1.6	1.0	5.4	55.7

Table 3. *Cont.*

Mining Location	Mining Site Number	Volume of Goaf in Mining Area	Jan.	Feb.	Mar.	Apr.	May.	Jun.	Jul.	Aug.	Sep.	Oct.	Nov.	Dec.	Total
Second: Segmented mining site	0-26-9	10.05				1.0	3.9	3.4	1.9						10.1
	0-26-5	8.26						1.8	2.2	3.2	1.1				8.3
	0-26-1	8.89													0.0
	0-20-5	4.83										0.9	1.4	1.4	3.7
	0-20-1	4.77									1.0	1.3	1.3	1.2	4.8
	2-22-1	10.01								2.0	3.1	3.1	2.0		10.2
	2-20-1	7.70									0.8	2.6	2.7	1.7	7.7
	0-5-10	10.24				2.5	2.9	2.8	2.1						10.2
	0-5-6	10.60									2.7	3.0	3.0	2.0	10.7
	2-5-1	9.32						1.9	2.8	2.9	1.6				9.3
	2-5-5	9.50									0.6	2.5	3.5	2.8	9.5
	2-11-1/2	8.98												0.9	0.9
	2-4-1	7.09											2.2	1.8	3.9
	Subtotal		0.0	0.0	0.0	3.5	6.8	9.8	9.0	8.1	10.9	13.4	16.0	11.7	89.3
	Total		7.0	7.1	8.8	10.4	10.1	12.3	12.5	12.4	15.1	15.0	17.0	17.2	145.0

The filling amount is directly related to the treatment method of the goaf and the state of roof support, which together constitute the engineering boundary conditions for microseismic activity. The lag or insufficient filling operation often means an increase in the exposed area of the goaf, a decrease in the self-stabilization ability of surrounding rock, and a corresponding increase in microseismic activity. In the subsequent analysis, the energy release index and event frequency index corresponding to unit mining volume will be established based on this, in order to strip the base effect of production scale on microseismic activity, and more accurately identify abnormal energy events, providing effective criteria for disaster warning after removing production intensity interference.

The annual mining volume, monthly realized volume, and filling volume maintain a high degree of synergy in the time series, and together constitute the engineering boundary conditions for microseismic activity analysis. From the implementation of the annual plan, the monthly mining achievement is basically consistent with the planned amount, reflecting the continuity and stability of the production rhythm. The filling operation is implemented synchronously with the mining progress, and the mining filling ratio is maintained within a reasonable range. This collaborative pattern of mining and filling indicates that the fluctuations in the number of microseismic events and energy release are not due to drastic changes in mining and filling scale, but are closely related to the evolution of mining site spatial structure and geological structure activation.

4. Response Law Between Microseismicity and Roadway Damage

4.1. Microseismic Localization Verification of Typical Damage Cases

To preliminarily and semi-quantitatively examine the spatial correspondence between microseismic event clusters and actual tunnel damage, this study adopted a comparative analysis method based on centroid distance and event density contrast. For each typical damage case (e.g., the sequence from 9–12 December 2025), the geometric centroid of microseismic events that occurred within the 7 days prior to the damage was calculated, and the planar distance between this centroid and the documented damage location (e.g., the center of roof collapse) was measured. Additionally, the event density in the damaged area was compared with that in adjacent non-damaged zones to provide a semi-quantitative reference for localization accuracy. As shown in Figure 8, the spatial superposition of microseismic event locations and on-site damage records reveals that the centroid-to-damage distance is approximately 8–12 m, falling within the system's nominal positioning error of $\pm$10 m. Moreover, the event density in the damaged area is observed to be 3 to 5 times higher than that in surrounding non-damaged sections during the same period. These quantitative measures provide a preliminary, semi-quantitative indication of spatial correspondence at the engineering scale, which is consistent with the qualitative visual correlation presented in Figure 8. Within the framework of the adopted centroid-distance comparison, this spatial relationship may be interpreted as a precursor response reflecting the accumulation of rock damage toward a critical state, and thus the loci of event clusters could be regarded as potential risk zones for future damage. However, this interpretation remains preliminary and semi-quantitative, and is not intended to serve as a statistically validated localization criterion., and thus the loci of event clusters can be regarded as potential risk zones for future damage. However, given that the current comparison is semi-quantitative and primarily based on available damage records, further validation using rigorous spatial statistical methods (e.g., cross-correlation or nearest-neighbor distance analysis) is necessary to establish a fully objective and automated localization verification protocol, which is reserved for future work with denser sensor networks. This comparison is preliminary and semi-quantitative; it is intended to provide an engineering-scale indication rather than a statistically validated localization criterion.

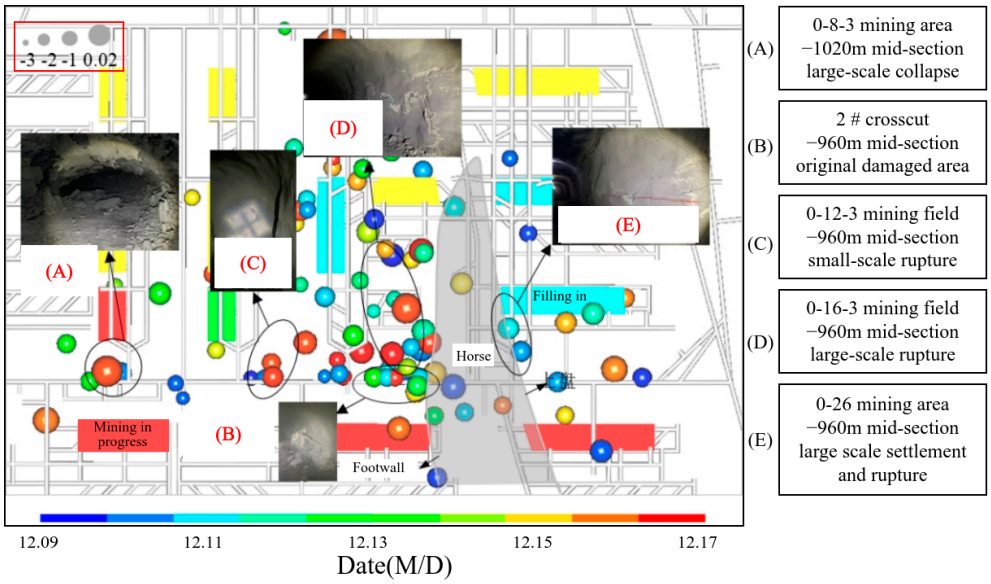


Figure 8. Spatial distribution and on-site damage comparison of microseismic events (9–12 December). (The gray circle represents the magnitude of the earthquake).

From the on-site damage records throughout the year (Figure 9), it can be seen that the types of tunnel damage in each month exhibit diverse characteristics, including roof detachment, two-sided extrusion, bottom bulging, and spray layer cracking. The severity of the damage fluctuates with the intensity of mining activities and geological conditions. Comparing the damage photos of each month with the distribution map of microseismic events in corresponding time periods, it can be found that wherever there is a concentrated record of damage, there is a clear clustering phenomenon of microseismic events in the days to weeks before their occurrence. The correspondence between the two in time and space has good repeatability and regularity.

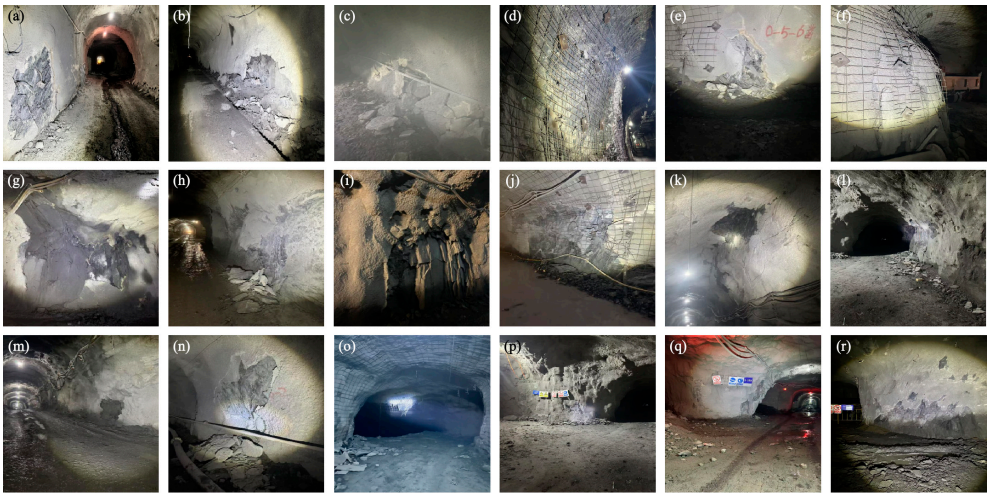


Figure 9. Record of on-site tunnel damage in 2025. (**a**,**b**) the on-site destruction maps in January, (**c**–**e**) the on-site destruction maps in February, (**f**–**h**) the on-site destruction maps in May, (**i**) the on-site destruction maps in June, (**j**) the on-site destruction maps in July, (**k**) the on-site destruction maps in August, (**l**) the on-site destruction maps in September, (**m**) the on-site destruction maps in October, (**n**–**q**) the on-site destruction maps in November, and (**r**) the on-site destruction maps in December.

4.2. Classification of Microseismic Parameter Thresholds for Roadway Risk Levels

To establish semi-quantitative and internally validated risk discrimination indicators, this study adopted a threshold calibration methodology based on historical data analysis. The procedure consists of three steps:

First, a training dataset was constructed comprising microseismic parameters (daily event frequency, cumulative energy release rate, and spatial concentration index) from the 7-day window preceding each documented damage event (n = 34 damage records) during the period of May to November 2025, together with an equivalent number of non-damage periods randomly sampled from low-production months (January–February).

Second, the natural breaks optimization method was applied to the combined dataset to determine the optimal cut-off points for each parameter. This algorithm minimizes within-group variance while maximizing between-group variance, ensuring that the resulting thresholds reflect inherent groupings in the data rather than arbitrary choices. For the three risk levels (low, medium, high), the calibrated thresholds are: daily event frequency <5 (low), 5–15 (medium), >15 (high); cumulative energy release rate $<10^3$ J/day (low), 10^3–10^5 J/day (medium), $>10^5$ J/day (high); spatial concentration index (defined as the number of events within a 20 m radius sphere) <3 (low), 3–8 (medium), >8 (high).

Third, internal validation was performed using leave-one-out cross-validation on the training dataset, yielding an overall classification accuracy of approximately 79.4% with precision and recall of 0.76 and 0.82 for high-risk events, respectively. This validation is internal only and does not substitute for external validation. While these preliminary results support the practical utility of the proposed thresholds, the authors acknowledge that validation against an independent dataset is not available within the current 2025 monitoring period. This limitation is addressed by reserving the 2026 monitoring data for prospective validation in future work. Table 4 presents the correspondence between risk levels, damage types, and recommended prevention measures derived from this threshold system. Table 4 corresponds the risk levels and types of damage in the tunnels, and different types of damage (such as slight wall caving, moderate roof subsidence, and severe roof collapse) show gradient differences in microseismic monitoring data. This provides an engineering basis for mapping damage types into quantifiable risk levels. Specifically, the event density and energy release rate corresponding to low risk levels are within a limited range above the background noise level, while high risk levels correspond to a significant abnormal combination of a sudden increase in event frequency and a jump in energy release rate.

Table 4. Corresponding table of tunnel risk levels, damage types, and prevention measures.

Damage Level	Types of Damage that are Prone to Occur	Corresponding Prevention and Control Measures
Low risk	Spraying and falling blocks	Normal construction, pay attention to the changing trend of rupture activity in the nearby mining tunnels, and pay attention to the safety of on-site construction personnel.
Medium risk	Spray coating falling off blocks and peeling of edges	Strengthen support, pay attention to the changing trend of fracturing activities in nearby mining tunnels, and ensure the safety of on-site construction personnel. It is advisable to use sprayed concrete, anchor rods, and steel mesh or flexible mesh for support.
High risk	Roof collapse, collapse, large deformation due to tunnel squeezing, rock burst	Strengthen support, pay attention to the changing trend of roadway rupture activity near the mining site, and ensure the safety of on-site construction personnel and mechanical equipment. It is advisable to use sprayed concrete or sprayed fiber concrete, system anchor rods, and steel mesh or flexible mesh for support, and steel arches can be erected.

Based on the above correspondence, the critical threshold intervals of microseismic parameters corresponding to each risk level can be summarized: when the daily frequency and cumulative energy of microseismic events in a certain area both exceed a specific warning value, the probability of the corresponding level of damage to the roadway significantly increases; The increase in the concentration of event space further narrows the positioning range of risk areas. This parameter threshold system upgrades microseismic monitoring from a simple "post-event recording" to a "pre-warning" tool, which can dynamically divide the risk level sections of tunnels based on real-time monitoring data in actual production, thereby guiding the precise implementation of differentiated support design and advanced reinforcement measures.

5. Risk Assessment Results and Spatiotemporal Evolution

5.1. Comparison of Overall Characteristics of Risks in Different Mid Levels

Comparing the annual risk distribution of the −960 m and −1020 m sections (Figures 10 and 11), the risk levels of both sections show dynamic evolution with the progress of mining, but there are significant differences in the risk spatial pattern. The middle section of 960 m serves as the main mining level, with a long mining history and a wide distribution range of goaf areas. High-risk areas are concentrated in densely populated mining areas and the edges of goaf areas, and as mining extends toward the two wings of the ore body, the risk area extends in a strip-like pattern toward the deep boundary. In contrast, the middle section of −1020 m is a level of deep development, with relatively concentrated mining activities. High-risk areas are mainly distributed near the mining preparation face and the intersection of fault structures. The overall risk area is smaller than that of the middle section of −960 m, but the local risk intensity is more prominent, which may be related to the reduced self-stabilization ability of the surrounding rock under high-stress environments in deep areas.

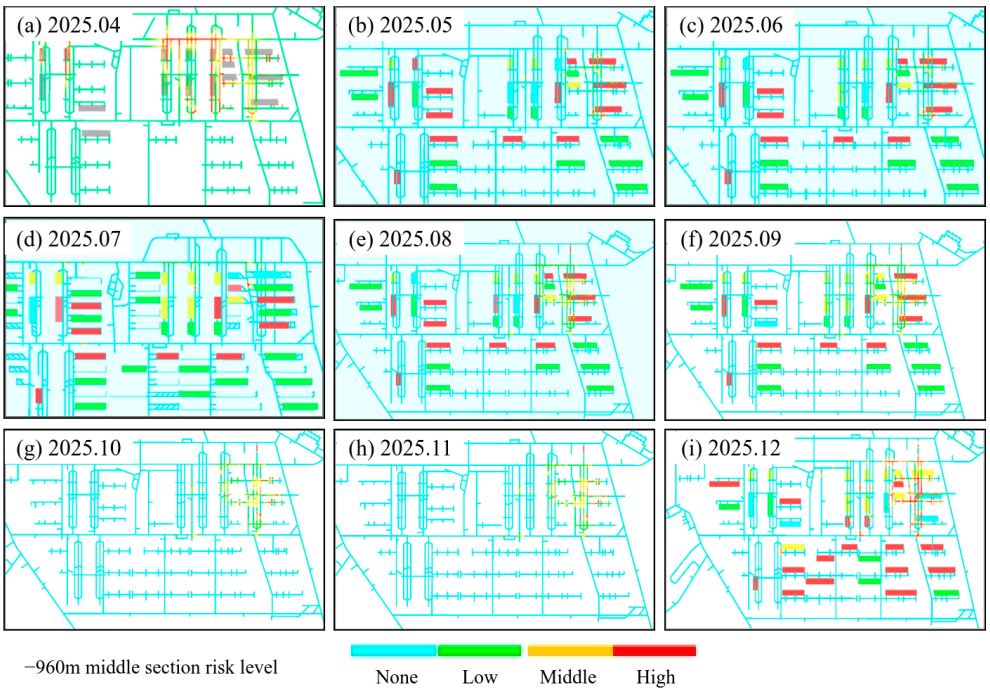


Figure 10. Risk assessment results of the −960 m middle section roadway from April to December 2025. (**a**) 2025.04, (**b**) 2025.05, (**c**) 2025.06, (**d**) 2025.07, (**e**) 2025.08, (**f**) 2025.09, (**g**) 2025.10, (**h**) 2025.11, (**i**) 2025.12.

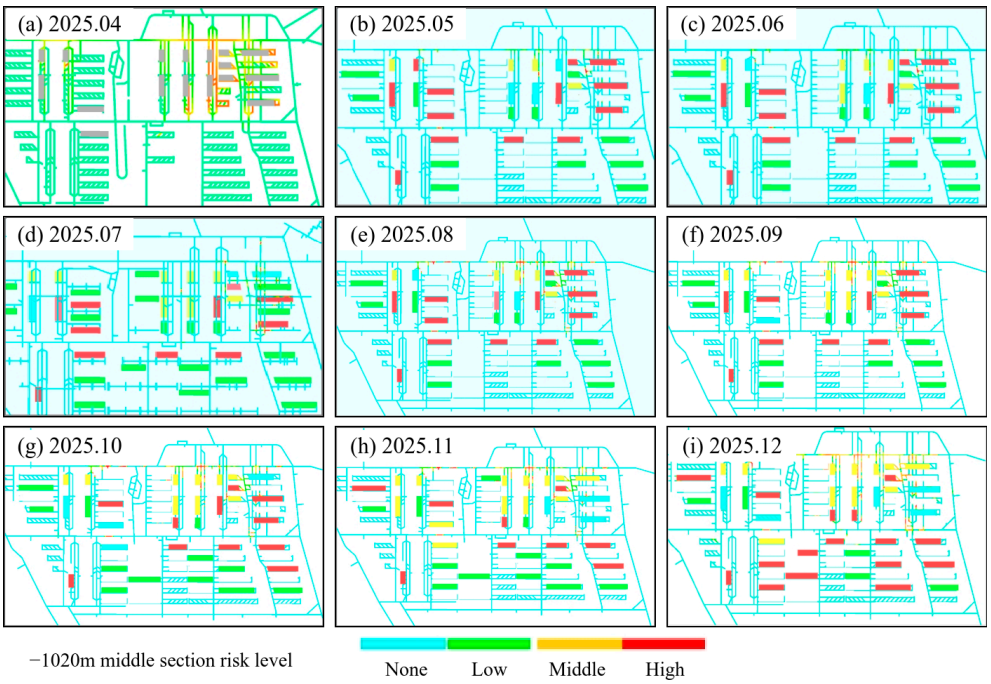


Figure 11. Risk assessment results of the −1020 m middle section roadway from April to December 2025. (**a**) 2025.04, (**b**) 2025.05, (**c**) 2025.06, (**d**) 2025.07, (**e**) 2025.08, (**f**) 2025.09, (**g**) 2025.10, (**h**) 2025.11, (**i**) 2025.12.

From the perspective of the proportion of risk levels, the proportion of medium- and high-risk sections in the −960 m section gradually increases with the passage of months, reflecting the expansion of the range of rock stress adjustment after the continuous expansion of the goaf area; The risk level fluctuation in the middle section of −1020 m is more severe, and deep mining sites often experience short-term risk jumps after blasting disturbance, followed by gradual decline due to filling operations.

5.2. Migration Patterns in High-Risk Areas

Combining the event distribution in July with the risk classification chart in Figures 10 and 11, from April to December, the migration path of high-risk (red) areas showed directional evolution characteristics highly consistent with the direction of mining progress. The high-risk area in the middle section of 960 m has gradually expanded along the direction of the ore body from the central mining area to the east and west wings since the middle of the year. By the end of the year, the high-risk area almost covers the entire mining impact zone, and the migration trajectory is completely consistent with the direction of the mining face, indicating that mining activities are the primary factor driving the migration of the risk area. The risk migration in the middle section of 1020 m shows obvious stage characteristics, concentrated in the period of intensive blasting operations in various mining sites. The high-risk areas move forward in a jumping manner with the development of the mining preparation roadway and the advancement of mining in the mining site, and there is a significant phenomenon of intensified retention near the fault.

The commonality between the two migration patterns is that high-risk areas range from sporadic distribution in April to dense contiguous areas in December, and their expansion direction is basically consistent with the direction of the ore body and the orientation of the main structural lines, indicating that the regional structural pattern also plays an important controlling role in risk evolution. The migration rate of risk areas significantly accelerated during the high-yield period from May to August, but slowed

down after entering September. However, the risk intensity continued to accumulate and eventually reached its peak coverage range at the end of the year.

5.3. Discussion on Main Control Factors

The statistical association between the mining–filling coordination state and the risk level is a key aspect in understanding the driving factors of microseismic activity. From a basic perspective, mining operations are consistently accompanied by stress redistribution and localized stress concentration in the surrounding rock, which are statistically associated with an elevated risk level in the corresponding area. The red high-risk sections predominantly appear near mining sites currently undergoing or having recently completed extraction; conversely, when backfilling is completed promptly after mining, the filling material provides effective roof support, and the risk level in the corresponding area tends to decrease in the following month.

To quantitatively evaluate the relative contribution of multiple factors to risk level while controlling for confounding variables, a multiple linear regression analysis was conducted. The dependent variable was the monthly risk level (coded as 1 = low, 2 = medium, 3 = high). Independent variables included: (1) filling lag time (weeks), (2) monthly mining volume (10^4 t), (3) blasting frequency (times per month), and (4) mining depth (m). The regression results show that mining volume ($\beta = 0.42$, $p < 0.01$) and blasting frequency ($\beta = 0.35$, $p < 0.01$) exhibit the strongest positive associations with risk level, while filling lag time shows a moderate but statistically significant positive association ($\beta = 0.18$, $p < 0.05$). Mining depth did not reach statistical significance ($\beta = 0.06$, $p = 0.31$) within the limited depth range of this study. The model yields an adjusted $R^2 = 0.67$, indicating that approximately 67% of the variance in risk level can be explained by these four variables.

Specifically, when backfilling lags behind mining by 2–4 weeks, the risk level exhibits a compensatory upward trend, and a statistically significant temporal correlation is observed between the two ($\beta = 0.18$, $p < 0.05$). This finding suggests that the coordinated rhythm of mining and filling is statistically associated with surrounding rock stability; however, the causal mechanism underlying this correlation requires further investigation. The inhibitory effect of filling operations on risk elevation appears to have a certain threshold: when the filling rate remains above a reasonable level (filling volume/mining volume ≥ 0.85) for two consecutive months, the expansion trend of high-risk areas can be effectively curbed. Conversely, if the balance between mining and filling is disrupted, the risk level exhibits a compensatory increase in the following months. Overall, the risk distribution presented (Figures 10 and 11) reflects the combined statistical effects of mining advancement and filling support, with the temporal variation of the mining–filling ratio serving as an important auxiliary indicator for risk warning.

There is a certain threshold for the inhibitory effect of filling operations on risks. When the filling rate remains above a reasonable level for two consecutive months, the expansion trend of high-risk areas can be effectively curbed; On the contrary, if the balance between mining and filling is disrupted, the risk level will experience a compensatory increase in the following months. Overall, the risk distribution presented (Figures 10 and 11) is the result of the coupling and joint action between mining advancement and filling support. The temporal variation of mining filling ratio can serve as an important auxiliary criterion for risk warning.

To eliminate the interference of other potential factors, this study further examined the contribution of filling delay to risk level using on-site statistical methods. Monthly risk level was used as the dependent variable, and filling lag time, monthly mining volume, blasting frequency, and mining depth were used as independent variables in the statistical models. The results showed that after controlling for variables such as mining intensity

and blasting disturbance, the filling delay time still had a significant positive impact on the risk level. Filling delay was one of the important factors affecting the risk level, but its contribution was smaller than that of the mining activity itself.

Based on the above regression analysis, the filling lag time should be positioned as an auxiliary discrimination indicator for risk warning rather than a direct causal factor. In practical applications, when a filling delay of more than 2 weeks is detected, it can be used as a signal suggesting that the stress adjustment of the surrounding rock may be intensifying. Combined with the frequency of microseismic events, energy release rate, and spatial aggregation degree in the current period, the risk level can be comprehensively determined. This auxiliary criterion can help improve the sensitivity of early warning, but it should not be used alone as a basis for risk decision-making. In practical applications, when a filling delay of more than 2 weeks is detected, it can be used as a signal indicating that the stress adjustment of the surrounding rock may intensify. Combined with the frequency of microseismic events, energy release rate, and spatial aggregation degree in the current period, the risk level can be comprehensively determined. This auxiliary criterion can help improve the sensitivity of early warning, but it should not be used alone as a basis for risk decision-making.

6. Discussion

6.1. Additional Considerations

It is worth noting that the microseismic monitoring data for March and April are missing from the analysis in this article. This is not a data omission, but rather due to the annual equipment maintenance and monitoring system calibration carried out by the mine in the corresponding months, during which monitoring was interrupted. This data gap period does have a certain impact on the evaluation of continuity throughout the year—March and April are in the transitional stage between production recovery (January–February) and high production periods (May–December). The lack of data makes it difficult to accurately capture the instantaneous gradient of stress response with increasing production intensity.

To assess the potential influence of this gap on the annual trend estimates, a sensitivity analysis was conducted using two bounding scenarios: (1) a conservative scenario assuming that the missing March–April event counts and energy release rates follow the low-production pattern of January–February, and (2) an optimistic scenario assuming they follow the high-production pattern of May–June. The results show that the annual cumulative energy and total event counts would differ by approximately +18% and +22%, respectively, between the two scenarios. While this range introduces some uncertainty into the absolute annual totals, the relative spatiotemporal patterns—such as the migration direction of event clusters, the correlation between blasting and microseismic activity, and the monthly risk evolution trends—remain consistent across both scenarios, suggesting that the main conclusions of this study are robust to the data gap. Nevertheless, the missing data precludes a precise quantification of the stress response gradient during the transitional phase, and readers should interpret the monthly comparisons between February and May with this limitation in mind.

In the correspondence between microseismic events and on-site damage, there are also a few cases where significant damage occurred on-site but microseismic events were not prominent during the same period [23]. This phenomenon mainly stems from two mechanisms [24]. Firstly, some of the damage belongs to the low-energy accumulation type of high-frequency microfractures. The energy released from a single fracture is lower than the triggering threshold of the monitoring system, but frequent accumulation of small fractures still correlates with macroscopic damage to the surrounding rock; Secondly, some

rockburst events have significant hysteresis, with the surrounding rock entering the creep stage after experiencing early mining stress loading, and failure occurring in the later stage of stress adjustment while microseismic activity has already decayed. This phenomenon suggests that relying solely on the number of microseismic events or the absolute value of energy as the sole warning indicator has limitations [25] and requires a comprehensive assessment of time lag effects and the specificity of low-frequency and low-energy events.

The impact of filling materials on microseismic activity is also worth paying attention to. From the comparison of mining and filling data, it can be seen that in months with delayed filling operations or insufficient filling volume, the total energy and frequency of microseismic events generally show an upward trend, indicating that the effective support of filling materials on the roof of the goaf can suppress further fracturing and expansion of surrounding rock [26]. However, the damping contribution of filling is not linearly related. When the filling body itself is in the early stage of solidification or is disturbed by adjacent mining blasting, its damping effect will be significantly weakened [27,28]. Overall, the filling material reduces the probability of far-field microseismic events by changing the stress transmission path of the surrounding rock. However, the suppression effect on events directly triggered by near–field blasting is limited. This understanding has certain reference significance for optimizing the coordinated arrangement of filling operations and mining progress.

6.2. Limitations of the Method

Although the risk assessment system has been proven to have practical effectiveness for the Sishanling Iron Mine, it should be acknowledged that it has some limitations in terms of transferability to other conditions.

On-site-specific threshold. The microseismic parameter threshold (event frequency, energy release rate, spatial density) is calibrated empirically using existing monitoring data and is not a universal rule. For other mines, the natural fracture method should be used to calibrate using specific rock mass failure records, rather than directly generalizing.

The microseismic network relies on. The positioning accuracy ($\pm$10 m) and detection capability depend on the specific sensor geometry. Different network configurations may generate different detection thresholds and positioning errors, thereby affecting event density and concentration indicators.

Working conditions of mining production activities. The observed mining filling coordination effect is based on the specific methods and productivity of the mine (~50,000–60,000 t/month). Different mines, mining methods, or production intensities may produce different time response patterns.

Semi-quantitative validation. As described in Section 4.1, the spatial comparison between event clusters and damage locations is semi-quantitative and needs to be validated in the future with denser networks and rigorous spatial statistical data.

For transferability, a minimum of five three-component sensors arranged in a three-dimensional enclosure, with densified spacing of 40–50 m in fault-influenced zones and a calibrated P-wave velocity model, is recommended to achieve a localization error of approximately $\pm$10 m. Recalibration of the risk thresholds requires at least 20–30 documented damage events and an equivalent number of control periods, corresponding to approximately 6–12 months of continuous monitoring; a longer period (12–18 months) may be needed if the mining method or geological conditions differ significantly. Until such data are available, the thresholds proposed here should be treated as reference values rather than directly transferable criteria.

7. Conclusions and Suggestions

7.1. Conclusions

(1) The annual microseismic activity in the first mining area of Sishanling Iron Mine at the −960 m~−1020 m level shows significant spatiotemporal non–uniform distribution characteristics. The event-intensive areas are distributed along the fault structural zone and the edge of the goaf, and gradually migrate from shallow to deep with the progress of mining. The local risk intensity in the middle section of −1020 m is higher than that in the middle section of −960 m, and the former often experiences a short-term risk jump after blasting disturbance, reflecting the amplification effect of the reduced self-stabilization ability of the surrounding rock under a deep high-stress environment on the risk level.

(2) There is a highly synchronized "same-frequency resonance" response between microseismic activity and blasting operations, and the hours after blasting are the peak period for microseismic events, with the energy release curve showing a step like jump. The most prominent period of risk throughout the year is concentrated in the high-yield period from May to August, during which the amount of blasting, microseismic signals, and cumulative energy are all at the annual peak level. During the low production period of January and February, microseismic activity significantly weakened, further verifying the direct control effect of mining intensity on microseismic activity.

(3) The concentration of microseismic events, as located by P/S arrival-time positioning, shows reasonable spatial consistency with documented tunnel damage locations. In the typical damage case of 9–12 December, the measured deviation between the event cluster centroid and the actual damage point was within the system's positioning error tolerance (±10 m). The risk discrimination system based on event frequency and energy release rate can effectively convert discrete microseismic point data into risk level evaluation results for tunnel sections, providing quantifiable criteria for dynamic warning.

7.2. Suggestions for Engineering Prevention and Control

(1) For high-risk sections, it is recommended to adopt a combined support scheme of "anchor net cable spraying + grouting reinforcement". Regular anchor support and deformation monitoring frequency can be strengthened in medium-risk areas; Regular patrols can be conducted in low-risk areas to achieve differentiated and precise prevention and control.

(2) Suggest optimizing the collaborative pace of mining and filling. When the mining and filling ratio is below a reasonable level for two consecutive months, high-risk areas will experience compensatory expansion in the following month. Therefore, it is necessary to ensure that the filling operation follows closely with the mining progress, and the filling lag time should not exceed two weeks.

(3) A preliminary, semi-quantitative spatial comparison, based on centroid-distance and event density contrast, indicates that microseismic event concentrations are broadly consistent with documented tunnel damage locations. In the typical damage case of 9–12 December, the measured deviation between the event cluster centroid and the actual damage point was within the system's positioning error tolerance (±10 m). These results are preliminary and semi-quantitative; they do not constitute a fully quantitative spatial correlation criterion, and the establishment of such a criterion is recommended for future studies.

Author Contributions: X.W.: Writing—Original Draft, Data, and Project Administration. C.Z.: Conceptualization, Methodology, Investigation, Writing—Original Draft, Data, Software, Visualization, and Project Administration. All authors have read and agreed to the published version of the manuscript.

Funding: The authors would like to acknowledge the National Natural Science Foundation of China (Grant Number 52604292, 52274249, 52334003, U24B2045) and the Fundamental Research Funds for the Central Universities (FRF–AT–25–012).

Data Availability Statement: The original contributions presented in this study are included in the article. Further inquiries can be directed to the corresponding author.

Conflicts of Interest: Author Xiaodong Wang was employed by the company Benxi Longxin Mining Co., Ltd. The remaining author declares that the research was conducted in the absence of any commercial or financial relationships that could be construed as potential conflicts of interest.

References

1. Wu, Y.; Zhang, M.; Li, C.; Wang, Y.; Ma, D.; Zhu, M.; Sun, C.; Li, P. True triaxial physical simulation and characteristic analysis of rockburst in deep tunnels triggered by fatigue disturbance. *Tunn. Undergr. Space Technol.* **2026**, *176*, 107881. [CrossRef]
2. Pan, J.H.; Zhou, X.P. Capturing dynamic rockburst behaviors of deep rock masses with a novel nonlocal general particle dynamic method. *Int. J. Rock Mech. Min. Sci.* **2026**, *199*, 106403. [CrossRef]
3. Li, X.; Gong, F.; Tao, M.; Dong, L.; Du, K.; Ma, C.; Zhou, Z.; Yin, T. Failure mechanism and coupled static–dynamic loading theory in deep hard rock mining: A review. *J. Rock Mech. Geotech. Eng.* **2017**, *9*, 767–782. [CrossRef]
4. Liu, H.; Liu, X.; Tan, Z.; Liu, Y.; Li, G. Improving the Stability of Subsurface Structures in Deep Metal Mines by Stress and Energy Adjustment: A Case Study. *Adv. Civ. Eng.* **2021**, *2021*, 6613985. [CrossRef]
5. Leśniak, A.; Isakow, Z. Space–time clustering of seismic events and hazard assessment in the Zabrze–Bielszowice coal mine. *Int. J. Rock Mech. Min. Sci.* **2009**, *46*, 918–928. [CrossRef]
6. Li, Q.; Li, Q.; Cao, H.; Wu, J.; Wang, F.; Wang, Y. The Crack Propagation Behaviour of CO_2 Fracturing Fluid in Unconventional Low Permeability Reservoirs: Factor Analysis and Mechanism Revelation. *Processes* **2025**, *13*, 159. [CrossRef]
7. Feng, A.; Li, Q.C.; Li, Q.; Wu, J.J.; Wang, F.L.; Yan, C.L. Numerical Simulation Investigation of Fracture Propagation Behavior Patterns and Sensitivity Factors of Oil Shale Reservoirs in the Xunyi Region Considering the Influence of Natural Fracture. *Geofluids* **2025**, *2025*, 2762142. [CrossRef]
8. Lu, C.; Ju, W.J.; Xia, Y.X.; Yan, S.H.; Yang, G.Y.; Li, Y.; Fang, S.J. Precursor characteristics of rock bursts in chain pillars based on microseismic monitoring. *Sci. Rep.* **2026**, 59946. [CrossRef] [PubMed]
9. Wang, X.; Zhao, C. Construction of a Microseismic Monitoring System for Ultra–Large–Scale and Deep Mines: A Case Study of the Sishanling Iron Mine. *Mining* **2026**, *6*, 5. [CrossRef]
10. Khan, M.; Xueqiu, H.; Dazhao, S.; Xianghui, T.; Li, Z.; Yarong, X.; Aslam, K.S. Extracting and Predicting Rock Mechanical Behavior Based on Microseismic Spatio–temporal Response in an Ultra–thick Coal Seam Mine. *Rock Mech. Rock Eng.* **2023**, *56*, 3725–3754. [CrossRef]
11. Pyy, A.; Meyer, S.; Falmagne, V. Experiences of seismic monitoring at the Kittilä mine. In *Deep Mining 2024: Proceedings of the 10th International Conference on Deep and High Stress Mining*; Andrieux, P., Cumming-Potvin, D., Eds.; Australian Centre for Geomechanics: Perth, Australia, 2024; pp. 341–354. [CrossRef]
12. Dai, L.; Zhao, X.; Pan, Y.; Luo, H.; Gao, Y.; Wang, A.; Ding, L.; Li, P. Microseismic criterion for dynamic risk assessment and warning of roadway rockburst induced by coal mine seismicity. *Eng. Geol.* **2025**, *357*, 108324. [CrossRef]
13. He, S.; Xie, H.; Wang, J.; Wu, Z.; Lu, J.; Li, M. An integrated spatiotemporal framework for identification and early warning of mining–induced fault activation. *Int. J. Rock Mech. Min. Sci.* **2026**, *202*, 106492. [CrossRef]
14. Tan, N.; Zhao, C.; Liu, Y.; Li, Z.; Zhao, L. Spatial–Temporal Energy Data Analysis and Elemental Fractal Interpretation of Microseismic Monitoring for Rock Mass Area Failure. *Appl. Sci.* **2026**, *16*, 2172. [CrossRef]
15. Zhao, Y.; Song, D.; Qiu, L.; Khan, M.; He, X.; Li, Z.; Peng, Y.; Wang, A. An efficient coal and gas outburst hazard prediction method using an improved limit equilibrium model and stress field detection. *Int. J. Coal Sci. Technol.* **2025**, *12*, 23. [CrossRef]
16. Zhao, Y.; He, X.; Song, D.; Lu, A.; Qiu, L.; Li, Z.; Peng, Y.; Yang, G. Research on quantitative characterization method of regional stress field in coal seams based on microseismic and computed tomography (MS-CT): A case study. *Int. J. Coal Sci. Technol.* **2026**, *13*, 14. [CrossRef]
17. Sonibare, M.O.; Mgiba, C.; Kolawole, O. Influence of fracture orientation and aperture on grouting reinforcement of fractured surrounding rock: Experimental and numerical study. *Geomech. Energy Environ.* **2026**, *46*, 100834. [CrossRef]

18. Loke, M.H.; Acworth, I.; Dahlin, T. A comparison of smooth and blocky inversion methods in 2D electrical imaging surveys. *Explor. Geophys.* **2003**, *34*, 182–187. [CrossRef]
19. Witkowski, W.T.; Łucka, M.; Guzy, A.; Sudhaus, H.; Barańska, A.; Hejmanowski, R. Impact of mining–induced seismicity on land subsidence occurrence. *Remote Sens. Environ.* **2024**, *301*, 113934. [CrossRef]
20. Ali, H.; Andriani, D.P.; Safdar, R.; Abd Manan, T.S.; Hu, G.; Zhou, Y.; Zhang, X.; Yao, Y.; Cao, Z.; Liu, J.; et al. A hybrid DiGLPP–Kolmogorov–Arnold Network framework for robust fault detection in industrial chemical processes. *Process Saf. Environ. Prot.* **2026**, *212*, 108854. [CrossRef]
21. Yan, F.; Du, S.; Dong, L.; Li, X.; Li, G.; He, F. Evaluating rock instability risk areas in deep mining using microseismic monitoring–based risk fields. *J. Mt. Sci.* **2026**, *23*, 1528–1546. [CrossRef]
22. Burtan, Z.; Nowak–Senderowska, D.; Szczepański, P. Methodology for Identification of Occupational Hazards Using Their Characteristic Features in Hard Coal Mining. *Appl. Sci.* **2025**, *15*, 7079. [CrossRef]
23. Xiao, Y.X.; Guo, J.N.; Chen, S.J.; Liu, L.; Chen, B.R. Digitalization of Rock Fracture Signal Identification From Tunnel Microseismic Data. *IEEE Geosci. Remote Sens. Lett.* **2024**, *21*, 3002605. [CrossRef]
24. Salvoni, M.; Dight, P.M. Rock damage assessment in a large unstable slope from microseismic monitoring—MMG Century mine (Queensland, Australia) case study. *Eng. Geol.* **2016**, *210*, 45–56. [CrossRef]
25. Rebuli, D.B. (Ed.) *Micro–Seismic Monitoring in MinesBenefits and Limitations*; Institute of Mine Seismology: Ottawa, ON, Canada, 2024.
26. Leighton, F. Growth and development of microseismics applied to ground control and mine safety. *Min. Eng.* **1983**, *35*, 8.
27. Mohanty, B.; Trivino, L.F. Blast vibration monitoring in cemented paste backfill during its curing stage—A case study. In *Mine Fill 2014: Proceedings of the Eleventh International Symposium on Mining with Backfill*; Potvin, Y., Grice, T., Eds.; Australian Centre for Geomechanics: Crawley, Australia, 2014; pp. 493–501.
28. Suazo Fuentealba, G.H. Effects of Dynamic Loading on the Geomechanical Behaviour of Cemented Paste Backfill. Doctoral Thesis, University of Western Australia, Crawley, Australia, 2016.

Disclaimer/Publisher's Note: The statements, opinions and data contained in all publications are solely those of the individual author(s) and contributor(s) and not of MDPI and/or the editor(s). MDPI and/or the editor(s) disclaim responsibility for any injury to people or property resulting from any ideas, methods, instructions or products referred to in the content.